Steady flow regimes and mixing performance in arrow-shaped micro-mixers

A. Mariotti, C. Galletti,* E. Brunazzi,† and M. V. Salvetti
Dipartimento di Ingegneria Civile e Industriale, University of Pisa, 56122 Pisa, Italy

(Received 6 August 2018; published 4 March 2019)

The different flow regimes occurring for increasing Reynolds numbers (Re) in an arrow-shaped micro-mixer operated for liquid mixing are investigated by the synergic use of experimental flow visualizations and direct numerical simulations. The tilting angle of the arrow-mixer inlet channels with respect to those of the T-shaped mixer is $\alpha = 20^\circ$. Consistent with previous studies in the literature, it is found that the onset of the engulfment regime, and consequently the sharp increase of the degree of mixing between the two flow streams, occurs at a lower Reynolds number than for a T-mixer operating in the same conditions. However, in contrast to what is observed for T-mixers, the degree of mixing does not increase monotonically with Re. In fact, at approximately $\mathrm{Re} = 150$, based on the inlet bulk velocity and the hydraulic diameter of the mixing channel, there is a drop of the mixing degree. This is due to a change in the topology of the vorticity field and, in particular, to the presence of a unique vortical structure in the mixing channel instead of two corotating ones typical of the engulfment regime. By further increasing the Reynolds number, the vortical structure in the mixing channel grows in size and eventually starts to oscillate, leading again to an increase of the degree of mixing, starting from $\mathrm{Re} \simeq 170$. Additional simulations have been carried out in order to investigate the sensitivity to the tilting angle of the inlet channels, namely for $\alpha = 10^\circ, 15^\circ, 25^\circ$. As expected, it is found that the value of Re at which the engulfment regime occurs decreases with increasing α. Then, for $\alpha = 10^\circ$ and 15°, the degree of mixing monotonically increases with the Reynolds numbers and the flow topology in the whole engulfment regime is practically the same as for T-mixers. Conversely, the configuration with $\alpha = 25^\circ$ shows a behavior of mixing and of flow features with increasing Reynolds number very similar to those observed for $\alpha = 20^\circ$.

DOI: 10.1103/PhysRevFluids.4.034201

I. INTRODUCTION

Liquid mixing is one of the key operations in engineering as fast and homogeneous mixing of reactants is a critical step for reactions, dissolutions, precipitations, and separations. Micro-mixers, constituted by submillimeter channels, have been proposed in the past decade as they allow continuous operation with an unprecedented control over mixing and residence time. One of the main advantages is the enhanced heat transfer capacity due to the high surface-to-volume ratio. This feature, for instance, enables safe operation with highly exothermic reactions, thus expanding the number of feasible reactions and conditions that can be run [1,2]. Moreover, continuous flow reduces accumulation of reactive or toxic intermediates. Hence, microfluidic devices are thought to provide significant economic, environmental, and safety benefits for many applications in fine chemistry and pharmaceutical processes, that have been proposed in addition to more traditional laboratory-on-chip applications [3]. Since the characteristic dimensions are small, the flow is

*Corresponding author: chiara.galletti@unipi.it
†Corresponding author: elisabetta.brunazzi@unipi.it

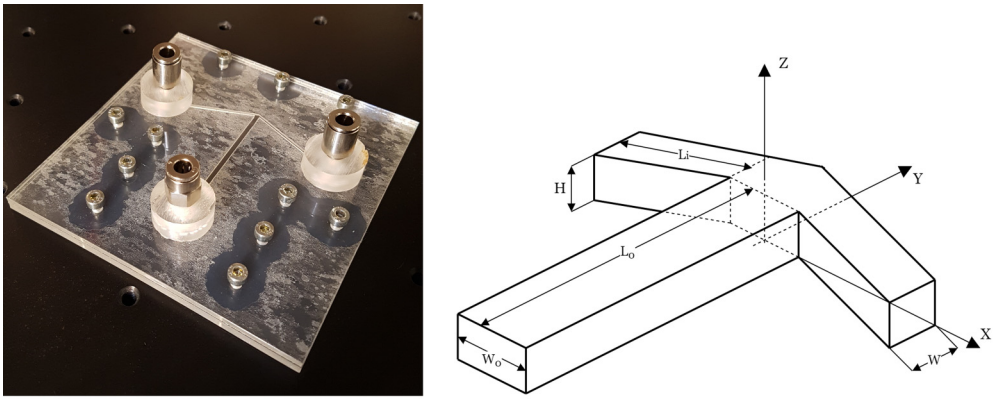

FIG. 1. Experimental model (a) and sketch of the arrow mixer with $\alpha = 20^\circ$ (b).

laminar, so mixing should be improved by using special enhancing methods that can be either active or passive [4,5]. The formers use an extra energy input, such as ultrasound, electric field, pressure pulse, etc. Passive methods instead promote mixing by exploiting special designs of the micro-mixer geometry aimed at breaking the flow symmetries; hence, they do not need any external energy input.

Among passive micro-mixers, the T geometry, in which the operating fluid enters the two aligned side channels and then is convected in the mixing channel, having its axis perpendicular to that of the inlet ones, is the most widely used because of its simplicity. For instance, it is often found as

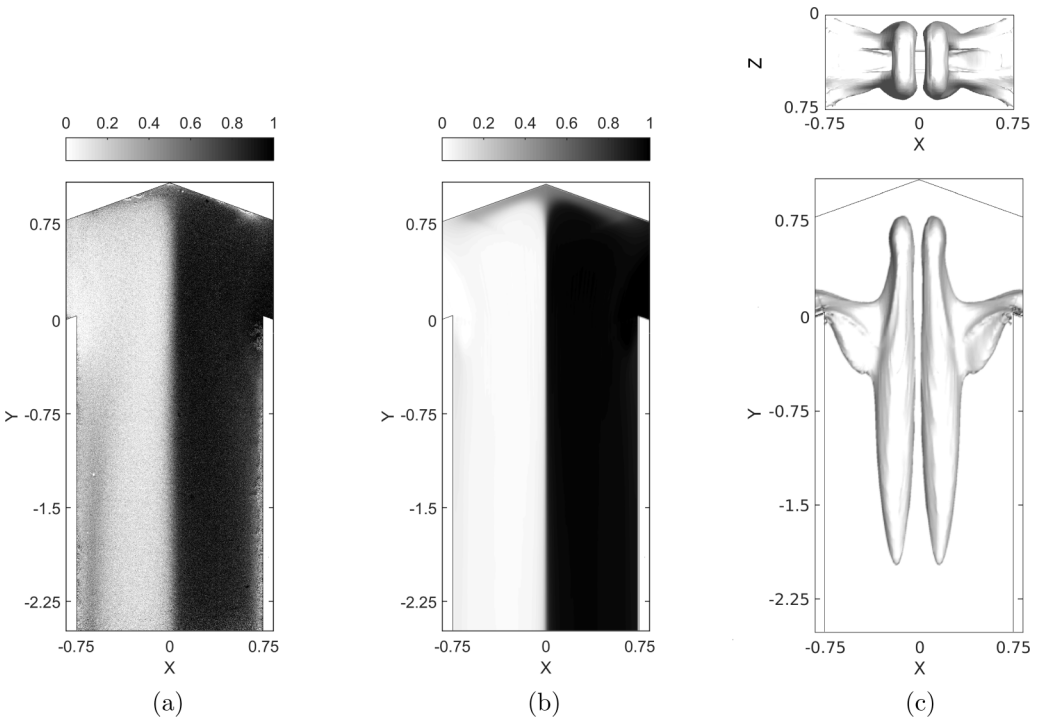

FIG. 2. Experimental (a) and numerical (b) dye concentration fields and isosurface of the λ_2 vortex indicator (c) for the arrow mixer with $\alpha = 20^\circ$ at Re $= 120$.

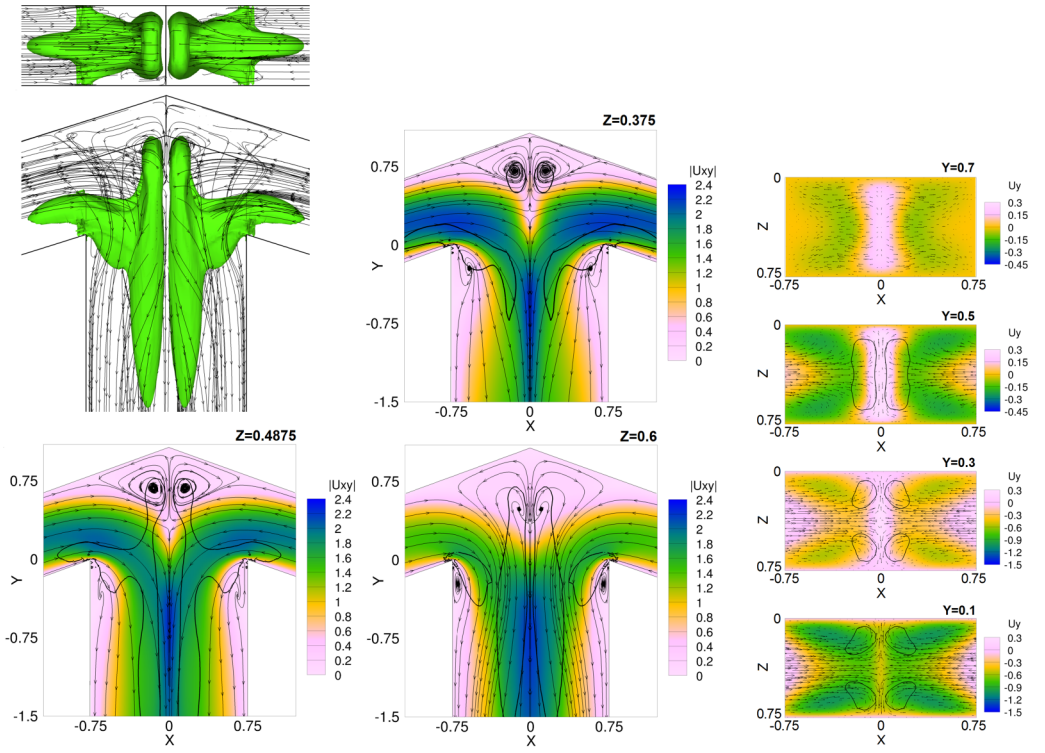

FIG. 3. Flow features in the top part of the arrow mixer with $\alpha = 20^\circ$ at Re $= 120$: (a) isosurface of the λ_2 vortex indicator and velocity streamlines (top left), contours of the in-plane velocity magnitude, velocity streamlines, and trace of the isosurface of the λ_2 (thick line) for the sections at $Z = 0.375$ (top right), $Z = 0.4875$ (bottom left), and $Z = 0.6$ (bottom right); (b) contours of the y velocity, in-plane velocity vectors, and trace of the isosurface of the λ_2 (thick line) for the cross sections at (from top to bottom) $Y = 0.7$, $Y = 0.5$, $Y = 0.3$, and $Y = 0.1$.

junction element in more complex micro-mixer networks. This micro-mixer configuration is also suited to carry out fundamental studies. Indeed, the flow behavior and the mixing efficiency of T-mixers have been largely investigated in the literature. In particular, different flow regimes have been identified as functions of the characteristic flow Reynolds number, Re, usually based on the inlet bulk velocity and on a characteristic length of the mixing channel, e.g., its hydraulic diameter. At very low Re, the two fluid streams flow side by side through the mixing channel, resulting in a completely segregated pattern (stratified regime). After increasing Re, in the vortex regime, a double pair of counter-rotating vortical structures originate in the region of confluence of the two streams and they form four legs of equal strength in the mixing channel. Since the flow in the vortical regime preserves the geometrical reflectional symmetries, mixing still occurs only through diffusion and, hence, it remains very low. After further increasing Re, the onset of the so-called engulfment regime takes place. In this regime, a tilting of the vortical structures at the top of the mixer is observed, which leads to symmetry breaking. Consequently, the two legs of each vortex entering the mixing channel are not equal in terms of intensity and, moving toward the end of the mixing channel, only two corotating vortical structures survive. A sudden increase of the degree of mixing is associated with the onset of the engulfment regime, so that many efforts in literature have been devoted to predicting the critical Re at which it occurs and at understanding its dependence on geometric parameters [6–9], flow conditions [10–12] and fluid properties [7,13–15].

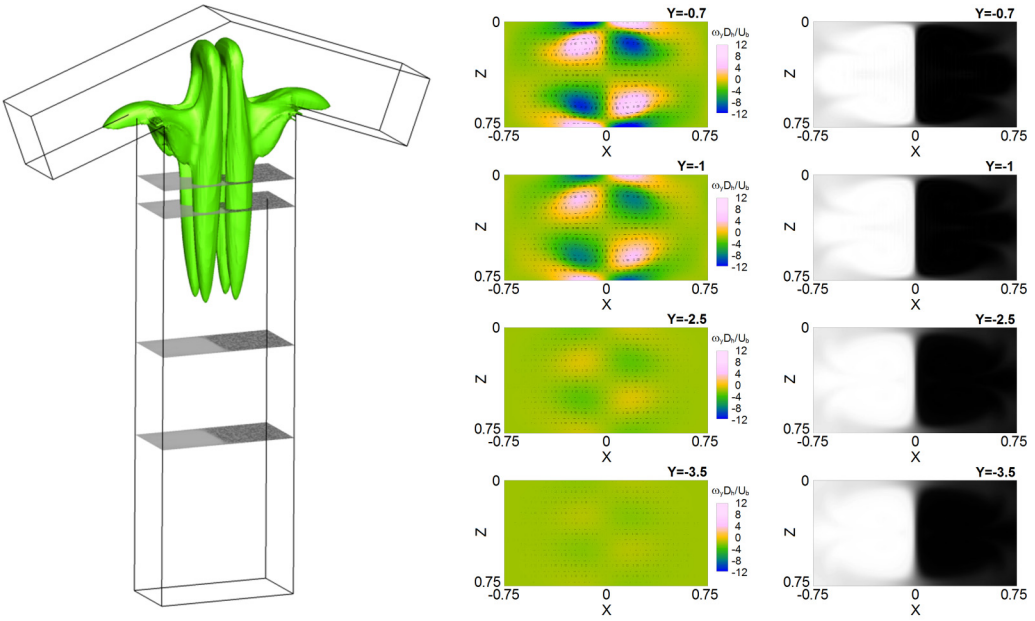

FIG. 4. Isosurface of the λ_2 vortex indicator from a different view (a), y vorticity and in-plane velocity (b), and dye concentration fields (c) for the arrow mixer with $\alpha = 20^\circ$ at $\mathrm{Re} = 120$. Considered cross sections (from top to bottom): $Y = -0.7$, $Y = -1$, $Y = -2.5$, and $Y = -3.5$. All the results are from numerical simulations.

As for the geometrical parameters, the effects of varying the aspect ratio of the channel have been investigated in Refs. [6–9], showing that this parameter may have a significant impact on the engulfment onset. Other modifications of the T-mixer geometry, aimed at facilitating the onset of the engulfment regime, and, in general, at enhancing mixing, have also been considered in the recent literature [16–20]. In particular, it was found in Ref. [19] that if the axis of the inlet channels is inclined downward with respect to the mixing channel, in order to obtain an arrow-shaped micromixer, the onset of the engulfment regime and thus efficient mixing performance can be obtained at Reynolds numbers significantly lower than for T-mixers. It was also shown in Ref. [19] that Y-shaped mixers are conversely characterized by the opposite trend; i.e., the onset of the engulfment regime occurs at larger Reynolds numbers than for T-mixers. The stability analysis in Ref. [19] showed that the differences observed in the flow field for varying the angle between the axis of the inlet channel and the one of the mixing channel, although confined in a small zone, are indeed located inside the core of the instability, i.e., the space region where the instability leading to the engulfment onset originates. This explains the significant effect of even small variations of this angle on the critical Reynolds number value. The simulations in Ref. [20] confirmed that the Reynolds number at which complete mixing is achieved in an arrow-shaped mixer is lower than for a T-mixer. However, Galletti *et al.* [21] observed through numerical simulations a drop in the degree of mixing when the Reynolds number is increased after the onset of the engulfment regime; this decrease in mixing seems to be associated with a change in the topology of the flow and, in particular, of the vorticity field.

The present work is motivated by the results of Ref. [19]. Since most of the previously mentioned applications take advantage of a large mixing occurring at low Reynolds numbers, we focus on arrow-shaped mixers, and, in particular, on the largest value of the tilting angle of the mixer inlet channels considered in Ref. [19], $\alpha = 20^\circ$. The investigation in Ref. [19] is limited to Reynolds numbers slightly larger than that at which the engulfment regime takes place. Therefore, we carry

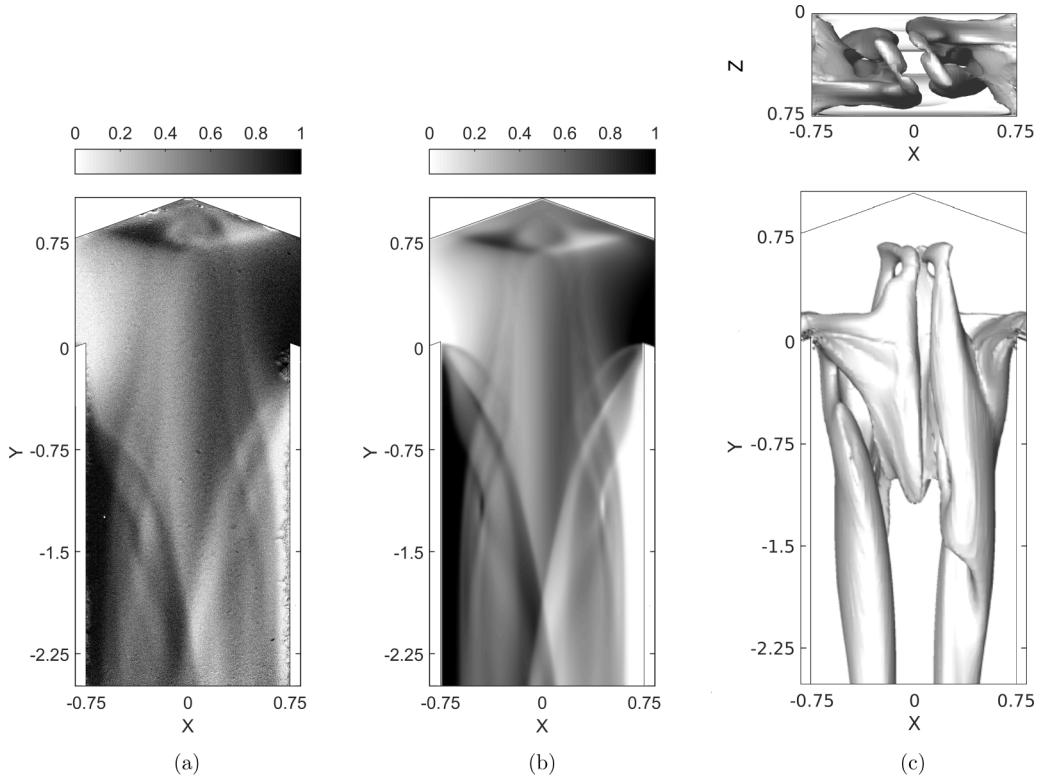

FIG. 5. Experimental (a) and numerical (b) dye concentration fields and isosurface of the λ_2 vortex indicator (c) for the arrow mixer with $\alpha = 20^\circ$ at Re = 140.

out herein a systematic and detailed analysis of the flow behavior and mixing performance of this arrow-shaped micro-mixer with increasing Reynolds number up to the onset of unsteady regimes. Direct numerical simulations are used together with experimental flow visualizations. The main goals are (i) to provide a full characterization of the flow and mixing behavior starting from the vortex regime up to Reynolds number values at which the flow becomes unsteady, (ii) to explain the observed behavior in terms of flow topology and physics, and (iii) to provide an experimental support to the characterization of flow regimes obtained in numerical simulations, similarly to what was done in Refs. [22,23] for T-mixers.

II. EXPERIMENTAL SET UP

The experimental model is made of polymethylmethacrylate (PMMA) and is shown in Fig. 1(a). A sketch of the arrow-mixer geometry is reported in Fig. 1(b), together with the adopted frame of reference. The inlet channels have a square cross section, with $W_i = H = 1$ mm, while the mixing channel presents a 2 : 1 aspect ratio, i.e., $W_o = 2H = 2$ mm, so that its hydraulic diameter is $d = 4H/3$. The length of the inlet channels, $L_i = 40$ mm $\approx 30d$, is enough to allow a fully developed flow at the confluence while the length of the mixing channel is $L_o = 60$ mm $\approx 45d$. The angle between the axis of the inlet channels and the x axis [see Fig. 1(b)] is $\alpha = 20^\circ$.

The mixer inlets are fed with deionized water streams with equal flow rates, corresponding to a bulk velocity of U, using a KD Scientific syringe pump. The bulk velocity in the mixing channel is therefore also equal to U. In order to differentiate the two streams and visualize the mixing process, one inlet stream is colored with a food colorant (E124), dissolved with concentration of 1.9×10^{-3} M. The mixing of the streams inside the arrow mixer was observed with an upright microscope

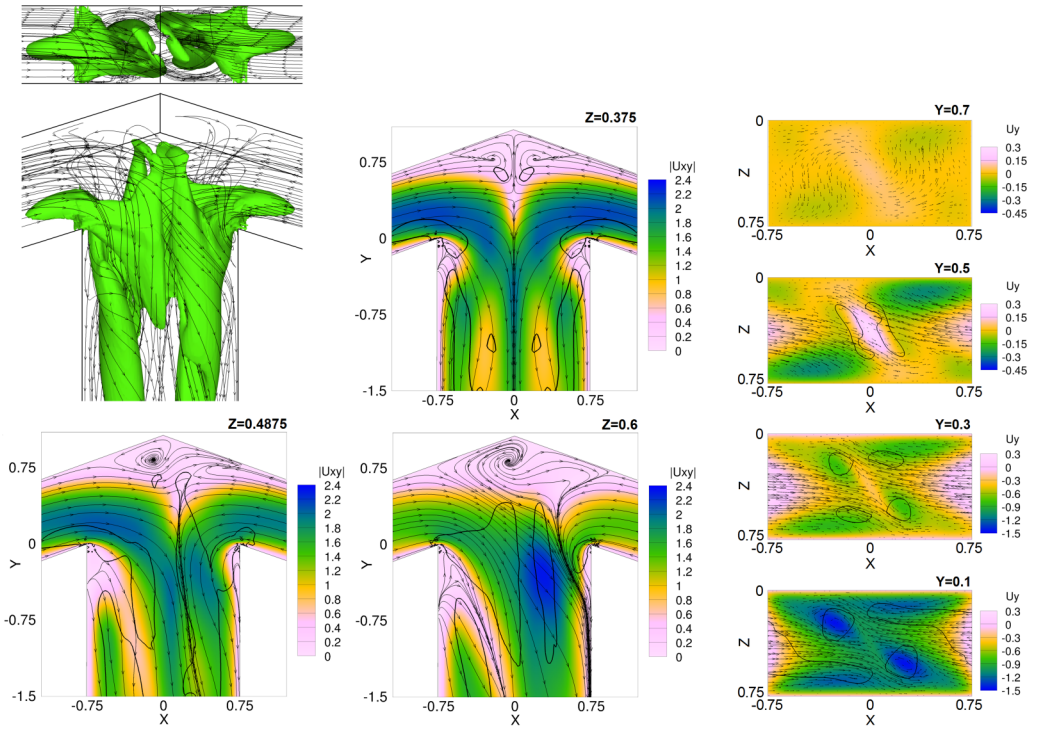

FIG. 6. Flow features in the top part of the arrow mixer with $\alpha = 20^\circ$ at Re $= 140$: (a) isosurface of the λ_2 vortex indicator and velocity streamlines (top left), contours of the in-plane velocity magnitude, velocity streamlines, and trace of the isosurface of the λ_2 (thick line) for the sections at $Z = 0.375$ (top right), $Z = 0.4875$ (bottom left), and $Z = 0.6$ (bottom right); (b) contours of the y velocity, in-plane velocity vectors, and trace of the isosurface of the λ_2 (thick line) for the cross sections at (from top to bottom) $Y = 0.7$, $Y = 0.5$, $Y = 0.3$, and $Y = 0.1$.

with a magnifying lens of $4\times$ and an aperture value setting equal to $N.A. = 0.13$. The light source is a D-LH 12V-100 W halogen lamp and all the experiments were performed in a dark room in order to maintain a constant level of luminosity with time and to minimize any reflections and shadows. The images were collected by using a high-speed camera having a monochrome sensor; for the investigated flow regimes, a resolution of 920×2048 pixels and a frame rate up to 387 frames/s were employed. The exposure time of each image is equal to $\delta T = 10^{-6}$ s, thus three orders of magnitude smaller than the sampling frequency. The interaction of light with the fully dissolved dye molecules was verified to obey the Lambert-Beer's law stating that the absorbance is linear with the concentration; hence, flow visualization images were processed off-line to convert pixel intensities into normalized depth-averaged dye concentration images. Details on the calibration and image analysis procedures can be found in Ref. [22], together with a more detailed description of the whole experimental setup.

III. NUMERICAL SIMULATIONS

The liquid motion is described by the unsteady incompressible nondimensional form of the Navier-Stokes equations (omitted here for the sake of brevity). The hydraulic diameter of the outlet channel, d, is used as a reference length, while the reference velocity is the bulk velocity, U, which is constant throughout the mixer. Therefore, the Reynolds number is defined as $\mathrm{Re} = \rho U d/\mu$, where

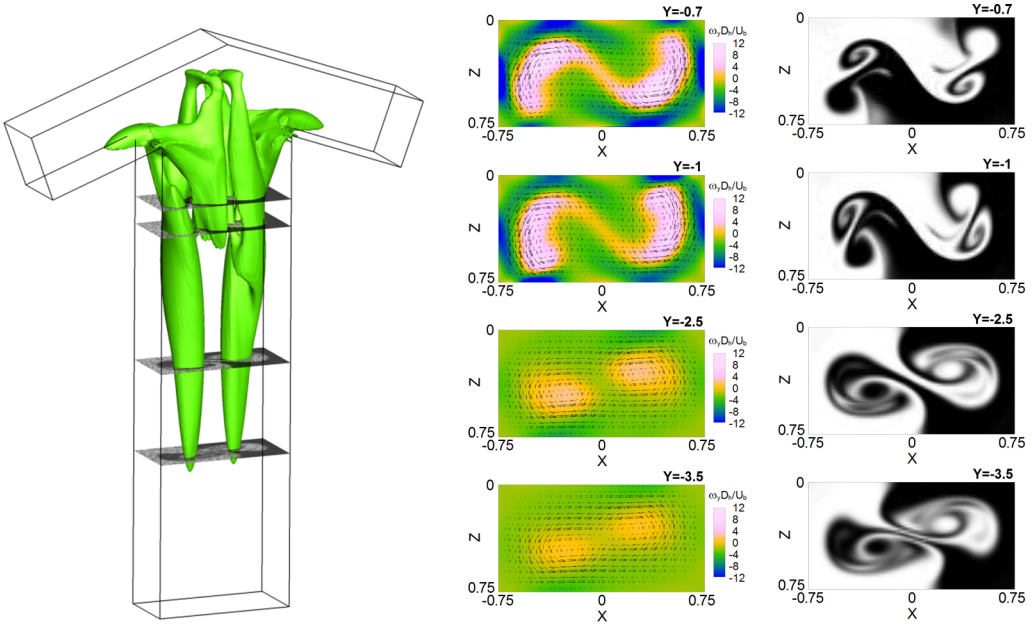

(a) (b) (c)

FIG. 7. Isosurface of the λ_2 vortex indicator (a), y- vorticity fields (b), and dye concentration fields (c) for the arrow mixer with $\alpha = 20^\circ$ at $\mathrm{Re} = 140$. Considered cross sections (from top to bottom): $Y = -0.7$, $Y = -1$, $Y = -2.5$, and $Y = -3.5$. All the results are from numerical simulations.

ρ and μ are the density and viscosity of the operating liquid. The Navier-Stokes equations are coupled with a transport equation governing the dye dynamics, which is written in the following nondimensional form:

$$\frac{\partial \phi}{\partial \theta} + \mathbf{u} \cdot \boldsymbol{\nabla} \phi = \frac{1}{\mathrm{Pe}} \nabla^2 \phi, \tag{1}$$

where ϕ is the dye mass fraction, θ is the nondimensional time, $\mathbf{u}$ is the nondimensional fluid velocity, and $\mathrm{Pe} = Ud/D$ is the Peclet number, with D denoting the dye molecular diffusivity. It is worth noting that for liquids the Schmidt number is very large, i.e., $\mathrm{Sc} = \mu/(\rho D) = O(10^3 \div 10^4)$, so that $\mathrm{Pe} = \mathrm{Sc}\ \mathrm{Re} = O(10^6)$.

The NEK5000 open-source code [24], based on a high-order spectral-element method, was employed to carry out the numerical simulations presented herein. The computational domain is discretized by means of hexahedral elements and the velocity space in each element is spanned by Nth-order Lagrange polynomial interpolants, based on tensor-product arrays of Gauss-Lobatto-Legendre (GLL) quadrature points. Time discretization is carried out by means of a third-order backward differential formula. The diffusive terms are treated implicitly, while a third-order explicit extrapolation is considered for the convective terms.

For the present simulations with $\alpha = 20^\circ$, the computational domain is the same as in the experimental model, except for the length of the inlet channels, which is lower, i.e., $L_i = 6.875d$. Hence, a unidirectional fully developed velocity profile is set at the inlets (see Ref. [6] for more details). The length of the mixing channel, $L_o = 25d$, is also less than that of the experimental model. Free outflow conditions are used at the outlet, by assuming zero normal gradient of the velocity components in the x and z directions and zero normal stresses. The sensitivity analysis carried out in Ref. [6] for a T-mixer geometry indicated that the adopted value of L_o together with the free outflow boundary conditions are adequate to avoid significant spurious effects of domain truncation. No-slip boundary

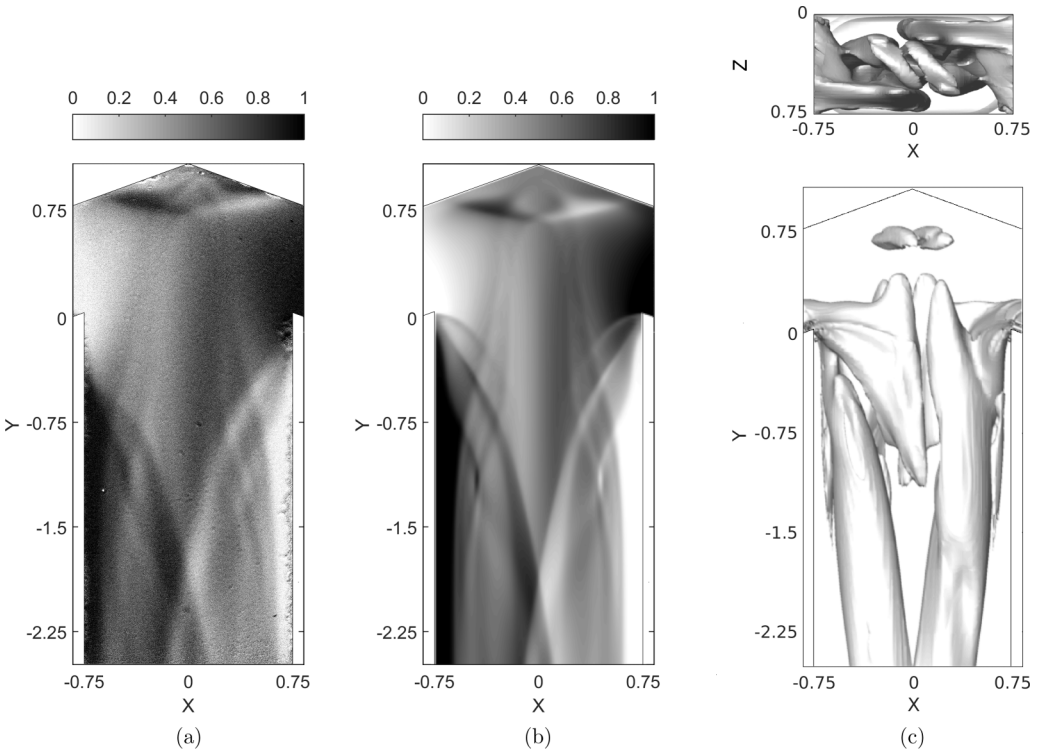

FIG. 8. Experimental (a) and numerical (b) dye concentration fields and isosurface of the λ_2 vortex indicator (c) for the arrow mixer with $\alpha = 20^\circ$ at Re $= 150$.

conditions are finally imposed at the mixer walls. The computational grid consists of 15 680 spectral elements, with a uniform element size of $0.075d$ in both directions of the cross sections of the mixer channels while along their axis the size varies between $0.08d$ and $0.5d$. The polynomial order N for the velocity is fixed to 6, while an order of 4 is adopted for the pressure, thus using the common P_N/P_{N-2} scheme, for a total of about 10^7 degrees of freedom for each velocity component. The time step is equal to $7.0 \times 10^{-4} \frac{d}{U}$, corresponding to a Courant-Friedrichs-Lewy (CFL) number $\leqslant 0.3$. This computational setup is practically the same as that used in the simulations in Ref. [19] for an arrow-shaped micro-mixer having a different aspect ratio. Arrow-shaped mixers having $\alpha = 10^\circ$, 15°, and 25° have also been simulated. The computational setup is the same as for $\alpha = 20^\circ$.

IV. RESULTS AND DISCUSSION

The experimental and numerical results obtained for different Reynolds numbers are presented in this section. In the following figures, all coordinates are made nondimensional by using the mixing channel hydraulic diameter, i.e., $X = x/d$, $Y = y/d$, and $Z = z/d$. The local dye concentration is normalized by the inlet concentration so that it ranges from 0 to 1. As for the dye concentration equation, in numerical simulations, stability issues forced us to use a rather low Sc number, i.e., Sc $= O(100)$, as in Ref. [25]. However, as shown in Ref. [26], such low Sc number does not affect the results in the confluence region analyzed in the present work, due to the presence of strong transversal convection. The numerical data were postprocessed on purpose to average the concentration field over the mixer depth, thus allowing the proper comparison with the experimental flow visualizations. More details are given in Ref. [22].

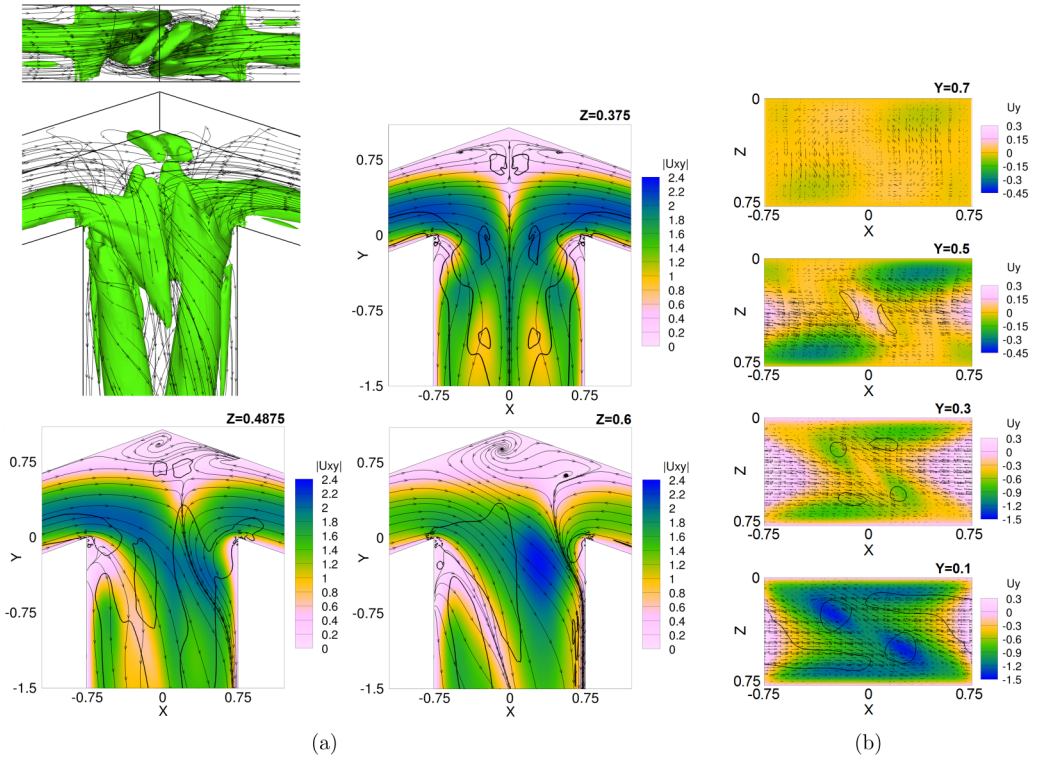

FIG. 9. Flow features in the top part of the arrow mixer with $\alpha = 20^\circ$ at Re $= 150$: (a) isosurface of the λ_2 vortex indicator and velocity streamlines (top left), contours of the in-plane velocity magnitude, velocity streamlines, and trace of the isosurface of the λ_2 (thick line) for the sections at $Z = 0.375$ (top right), $Z = 0.4875$ (bottom left), and $Z = 0.6$ (bottom right); (b) contours of the y velocity, in-plane velocity vectors, and trace of the isosurface of the λ_2 (thick line) for the cross sections at (from top to bottom) $Y = 0.7$, $Y = 0.5$, $Y = 0.3$, and $Y = 0.1$.

A. Vortex regime

Let us start by analyzing the results obtained at Re $= 120$. Figure 2(a) shows the steady depth-averaged dye concentration field from experimental flow visualizations, while the corresponding numerical concentration field is reported in Fig. 2(b). The agreement between experimental flow visualizations and numerical simulations is very good and, in both cases, at this low Reynolds number the two flow streams appear to remain segregated in the mixing channel. The three-dimensional vortical structures characterizing this regime are visualized in Fig. 2(c) by means of the λ_2 criterion [27]. According to this criterion, a vortex is defined as a connected fluid region where the second largest eigenvalue, λ_2, of the symmetric tensor $\mathbf{L} = \mathbf{S} \cdot \mathbf{S} + \mathbf{A} \cdot \mathbf{A}$ is negative, where $\mathbf{S}$ and $\mathbf{A}$ indicate the symmetric and antisymmetric parts of the velocity gradient that are the strain rate and vorticity tensors, respectively. The isosurface of λ_2 in Fig. 2(c) is 3D; for ease of comparison, the same 2D view as for the dye field visualizations is shown in the bottom panel, while a top view is provided in the top panel. The top parts of these structures are strictly related to the flow recirculations occurring near the top wall of the mixer at the confluence of the two streams entering the inlet channels; these recirculations can be clearly seen in Fig. 3(a). In more detail, part of the flow at the confluence of the streams is lifted up near the central plane of the mixer by the velocity induced by the top parts of the vortical structures; this leads to a saddle point in the streamlines in the x-y plane [see Fig. 3(a)]. The lifted-up fluid is in part directly convected downstream at the lateral

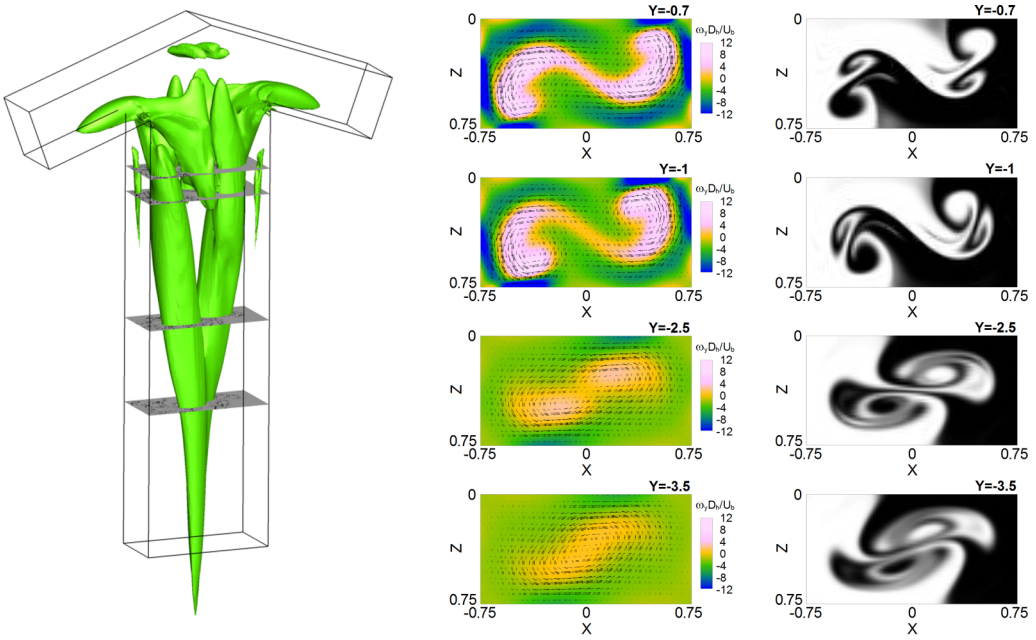

FIG. 10. Isosurface of the λ_2 vortex indicator (a) y- vorticity fields (b) and dye concentration fields (c) for the arrow mixer with $\alpha = 20^\circ$ at Re $= 150$. Considered cross sections (from top to bottom): $Y = -0.7$, $Y = -1$, $Y = -2.5$, and $Y = -3.5$. All the results are from numerical simulations.

edges of the vortex heads, closing in this way the recirculating regions, again shown in Fig. 3(a). However, part of it flows along the vortical structures and eventually is convected downstream in the mixing channel only when reaching the vicinity of the mixer walls parallel to the x-y plane [see also Fig. 3(b)]. This is in turn connected with the formation of two pairs of counter-rotating *legs* for each vortical structure (see also Fig. 4). For low Reynolds numbers, as the present one, the flow and the described vortices preserve the two reflectional geometrical symmetries in the whole domain and, in particular, also in the mixing channel (see Fig. 4). Consequently, convection does not help mixing, which occurs only through diffusion, and, as a result, the two streams remain segregated also in the mixing channel [Fig. 4(c)]. This scenario is typical of the vortex regime and, as found also in Ref. [19], it is qualitatively the same as the one observed and widely characterized in the literature for T-mixers (see, e.g., Refs. [6,10]).

B. Engulfment regime

As the Reynolds number increases, the flow in the mixer enters the so-called engulfment regime, as shown, for instance, in Figs. 5, 6, and 7 at Re $= 140$. The flow is still steady, but, looking at the concentration fields in Figs. 5(a) and 5(b), it is clear how the flow patterns in this regime are more complex and how the mixing between the two streams is largely increased compared to the vortex regime. The agreement between numerical simulations and experimental flow visualizations is once again very good.

Figure 6 shows the flow features in the top part of the mixer and, namely, the same quantities as in Fig. 3. A first observation is that the recirculation regions move closer to the top wall and to each other and become smaller as the Reynolds number increases. The same is for the top parts of the 3D vortical structures, which are tightly connected with the flow recirculations. More striking is the rupture of the double mirror symmetry of the flow. Indeed, it can be seen that the recirculation zones

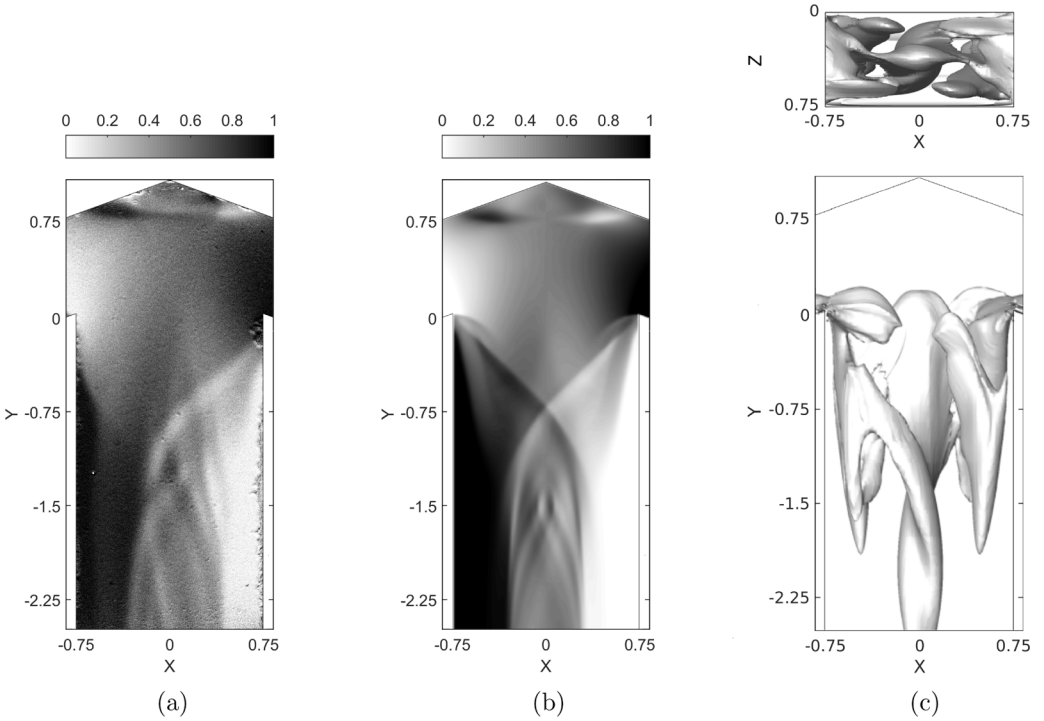

FIG. 11. Experimental (a) and numerical (b) dye concentration fields and isosurface of the λ_2 vortex indicator (c) for the arrow mixer with $\alpha = 20^\circ$ at Re $= 170$.

and the top parts of the vortical structures are tilted with respect to the z direction. As in the vortex regime, a fraction of the fluid entering the top part of the mixer, where inclined vortical structures are present, flows along them toward the side walls, before being convected downstream. However, now there is a preferential direction, which is that corresponding to the lower deviation angle. As a consequence, the amount of fluid which flows downstream at the two edges of each structure is significantly different and hence the two legs entering the outflow channel are not equal in terms of intensity, shape, and position. As can be better seen in Fig. 7, moving toward the end of the mixing channel, the weakest couple of legs disappears and only two main corotating vortices survive, which are further fed by the flow entering the channel directly below the recirculation regions. The signature of these complex vorticity structures can be identified in the dye concentration fields in Figs. 5(a) and 5(b): For instance, the two recirculation regions near the top walls are clearly visible and they appear slightly superimposed because of their tilting. Also, the strong vortex legs in the mixing channel are visible, while in the first part, roughly up to $Y = -1.9$, also the effects of the weakest legs can be identified. The previously described vorticity pattern is in agreement with the results of Ref. [19] and, once again, it is qualitatively the same as the one observed and widely characterized in the literature for T-mixers (see, e.g., Refs. [6,10]). The main difference with respect to T-mixers is that the onset of the engulfment regime occurs at lower Reynolds numbers, as found in Ref. [19]: Indeed, in the present case, the critical Reynolds number for the onset of the engulfment regime is found, both experimentally and numerically, to be between 125 and 130, while for a T-mixer having the same geometry of the channels and operating in the same conditions, the engulfment was found to establish for Re between 140 and 145 [22]. It is well known that mixing in the engulfment regime, thanks to the help of convection, is much larger than in the vortex one. This can be qualitatively appreciated by comparing Figs. 4(c) and 7(c) and it will be better quantified in Sec. IV C. The dye distribution in the mixing channel cross sections is only available in numerical simulations, because the experiments only give the concentration averaged through the

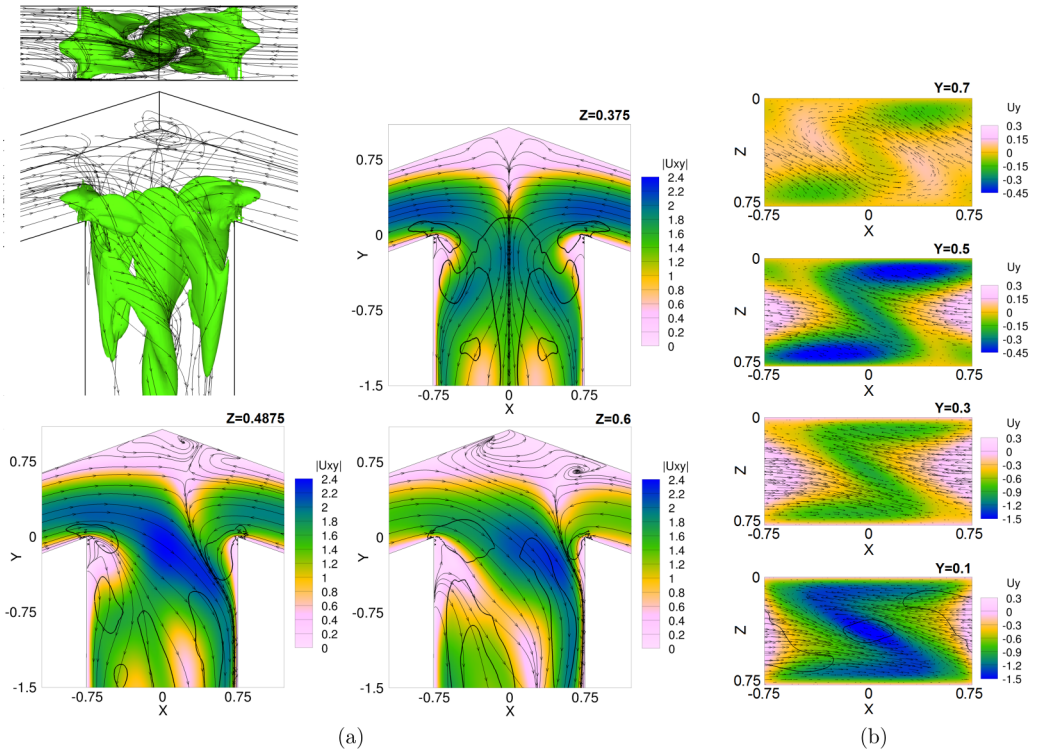

FIG. 12. Flow features in the top part of the arrow mixer with $\alpha = 20^\circ$ at Re = 170: (a) isosurface of the λ_2 vortex indicator and velocity streamlines (top left), contours of the in-plane velocity magnitude, velocity streamlines, and trace of the isosurface of the λ_2 (thick line) for the sections at $Z = 0.375$ (top right), $Z = 0.4875$ (bottom left), and $Z = 0.6$ (bottom right); (b) contours of the y velocity, in-plane velocity vectors, and trace of the isosurface of the λ_2 (thick line) for the cross sections at (from top to bottom) $Y = 0.7$, $Y = 0.5$, $Y = 0.3$, and $Y = 0.1$.

channel depth. Thus, we compared the depth-averaged concentration obtained at different sections throughout the mixing channel to the experimental one and the agreement was found to be very good (not shown here for the sake of brevity). From a practical viewpoint, the lower value of the Reynolds number at which the engulfment regime occurs makes the arrow-shape interesting.

Let us now further increase the Reynolds number. Figure 8 shows the steady dye concentration field and vortical structures at Re = 150, while the main flow features in the top part of the mixer are highlighted in Fig. 9. Starting from the dye concentration field, once again the agreement between experiments and numerical simulations is very good. The concentration field patterns in the mixing channel are qualitatively the same as at Re = 140, while the signatures of the flow recirculation regions in the top part of the mixer are now only hardly visible. This is because the recirculation zones further move toward the top wall compared to Re = 140 and become smaller and weaker. The same is for the top parts of the vortical structures, which in the present case appear to be disconnected from their legs. Also their tilting angle increases with Reynolds number, consistent with what was observed for T-mixers [6,10,22]. Apart from these differences, the flow pattern in the top part of the mixer is qualitatively the same as for Re = 140 with most of the fluid flowing along the vortex heads in the direction corresponding to the smaller deviation angle and then being convected downward in the mixing channel. As a result, two main corotating vortex legs are present in the mixing channel as at Re = 140 (Fig. 10). Compared with the case at Re = 140, these two corotating vortical structures tend to become closer to each other and eventually merge in the mixing channel (compare Figs. 10 and 7).

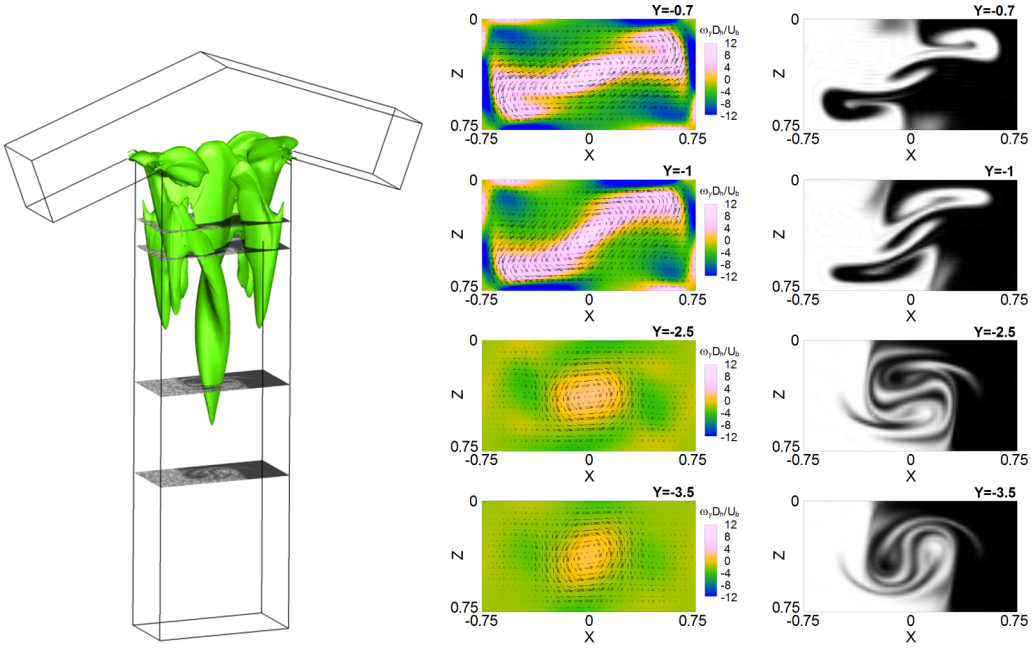

(a) (b) (c)

FIG. 13. Isosurface of the λ_2 vortex indicator (a), y-vorticity fields, (b) and dye concentration fields (c) at Re = 170. Considered cross sections (from top to bottom): $Y = -0.7$, $Y = -1$, $Y = -2.5$, and $Y = -3.5$. All the results are from numerical simulations.

Moving to Re = 170 (Figs. 11, 12, and 13), the flow is still steady but a gradual change in the flow topology can be noticed. The recirculation regions near the top wall have almost disappeared and consequently also the top parts of the vortical structures. This in turn implies that there is no more fluid lifted up in the center of the mixer; conversely, some of the fluid reaching the top part of the mixer undergoes a sort of spiral pattern near the center of the mixing channel and it is convected downward in this way. Such spiral pattern promotes the immediate merging, through clinging, of the two corotating vortical structures in the mixing channel. This leads to the presence of a single vortical leg in the mixing channel, as also shown in Fig. 13. This type of flow pattern is not found in T-mixers, in which the flow remains in the classical engulfment regime for Reynolds numbers up to Re $\approx$ 220 and then passes to an unsteady periodic behavior (see, e.g., Refs. [6,10,26,28,29]). Finally, it can be inferred from the dye field sections in Fig. 13 that the new flow topology is less efficient in promoting mixing than the classical engulfment one (compare, e.g., with Fig. 10). However, this will be quantified and discussed in Sec. IV C.

If we keep increasing the Reynolds number, the central vortical structure in the mixing channel increases in size and intensity (see, e.g., Figs. 14–16 for Re = 190). The dye distribution in different cross sections of the mixing channel well indicates that the strength of the central vortical structure leads to a spiral pattern, which is more effective in promoting mixing than for the Re = 170 case.

Finally, for Re $\geqslant$ 200, the flow becomes unsteady and periodic; the unsteady regimes will be the object of future investigations.

C. Mixing performance

To quantify mixing between the two streams, following Ref. [13], we use the mixing degree, δ_m, defined as follows:

$$\delta_m(Y) = 1 - \frac{\sigma_b(Y)}{\sigma_{\max}}, \tag{2}$$

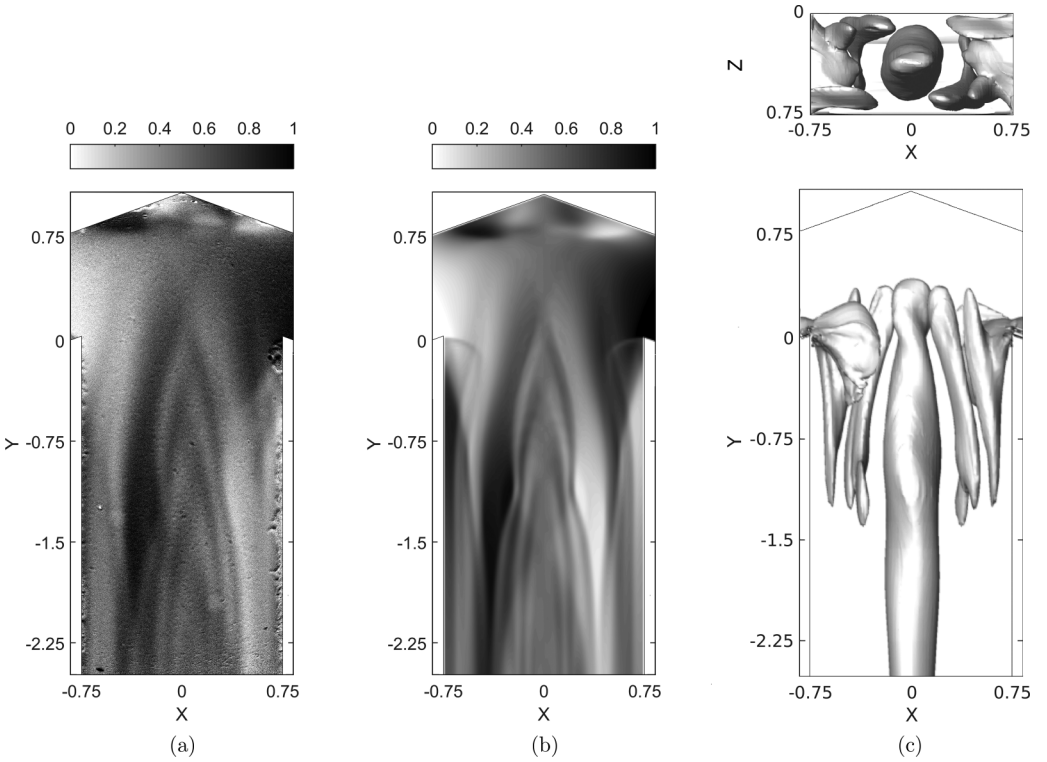

FIG. 14. Experimental (a) and numerical (b) dye concentration fields and isosurface of the λ_2 vortex indicator (c) for the arrow mixer with $\alpha = 20^\circ$ at Re = 190.

where σ_b is the standard deviation of the volumetric flow given by the following expression:

$$\sigma_b^2(Y) = \frac{\int (\phi(X,Y,Z) - \bar{\phi}_b)^2 u_y(X,Y,Z)\, dX\, dZ}{\int u_y(X,Y,Z)\, dX\, dZ}, \tag{3}$$

where $u_y(X,Y,Z)$ is the y-velocity component in the X-Z cross section of the mixing channel and the bulk or cup mixing average $\bar{\phi}_b$ is

$$\bar{\phi}_b = \frac{\int \phi(X,Y,Z) u_y(X,Y,Z)\, dX\, dZ}{\int u_y(X,Y,Z)\, dX\, dZ}. \tag{4}$$

Finally, $\sigma_{\max}$ is the maximum value of σ_b, which is achieved when the two streams remain completely segregated, and it is defined as

$$\sigma_{\max} = \sqrt{\bar{\phi}_b(1 - \bar{\phi}_b)}. \tag{5}$$

As a result, δ_m is bounded in the range $0 \leqslant \delta_m \leqslant 1$, $\delta_m = 0$, and $\delta_m = 1$, indicating a completely segregated and a fully mixed flow, respectively.

Figure 17 shows δ_m computed in numerical simulations at the $Y = -8$ section of the mixing channel as a function of the Reynolds number. The curve obtained for numerical simulations carried out with the same code for a T-mixer having the same geometry of the channels and operating in the same conditions [26] is also reported for comparison. Only Reynolds numbers at which the flow is steady are shown in Fig. 17; by further increasing Re, unsteady periodic regimes take place (see, e.g., Refs. [6,22,25] for T-mixers).

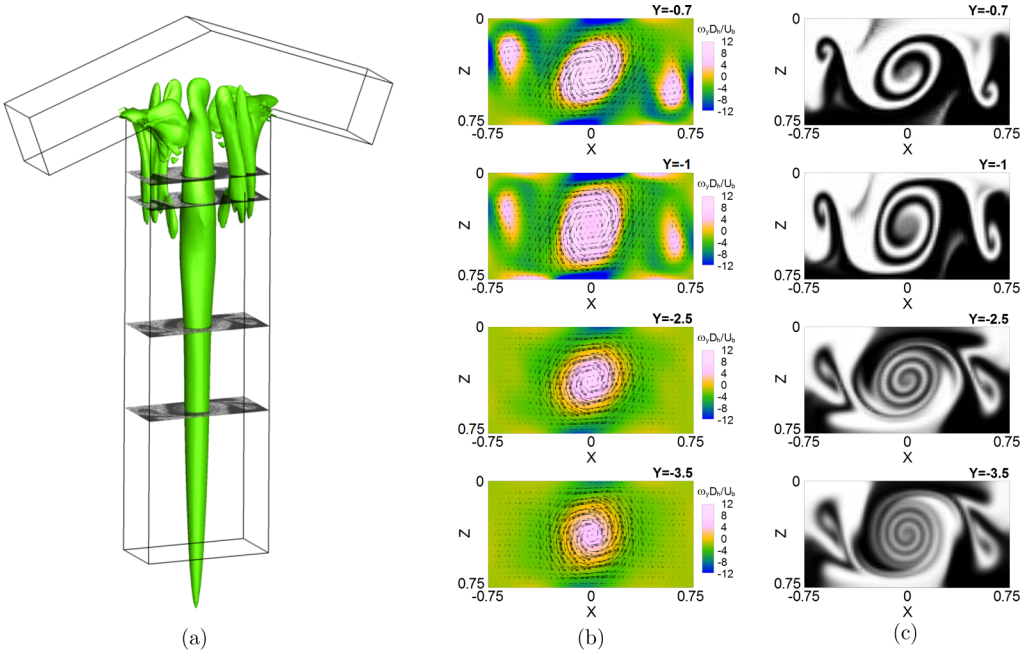

FIG. 15. Isosurface of the λ_2 vortex indicator (a), y-vorticity fields, (b) and dye concentration fields (c) for the arrow mixer with $\alpha = 20^\circ$ at Re $= 190$. Considered cross sections (from top to bottom): $Y = -0.7$, $Y = -1$, $Y = -2.5$, and $Y = -3.5$. All the results are from numerical simulations.

Figure 17 confirms and quantifies the previously made observations. A first sharp increase of the mixing degree can be seen at the onset of the engulfment regime, which, as previously said, occurs at lower Reynolds numbers for the arrow-shaped mixer than for the T-mixer. By further increasing the Reynolds number, in the arrow-shaped case, δ_m initially increases up to a local maximum approximately at Re $= 140$ and then drops, reaching a local minimum close to Re $= 170$. This decrease of δ_m is due to the previously described flow topology changes leading to the formation of a single vortical structure in the mixing channel, whose induced velocity field is less efficient than the two distinct corotating vortices present in the classical engulfment regime. Then, mixing increases again because this vortical structure expands in size and increases its intensity (see Re $= 190$). At approximately Re $= 200$, the vortical structure starts to oscillate and the flow becomes unsteady and periodic in time; hence, this Re is not reported in the figure. As previously said, the unsteady regimes will be investigated in detail in future works.

It is interesting to note that the behavior of δ_m in the steady engulfment regime for the T-mixer is instead monotonically increasing with Re and, despite the earlier increase of the mixing degree, there is a range of Reynolds numbers in which δ_m is lower in the arrow-shaped case. This suggests that a more accurate control of the operating conditions is needed for a arrow-shaped mixer than for a T-mixer, in order to obtain optimal mixing also within the engulfment regime.

D. Sensitivity to the tilting angle of the inlet channels

We finally analyze the sensitivity to α by means of additional simulations. Let us start with the behavior of the degree of mixing as a function of the Reynolds number, shown in Fig. 18. The results for the T-mixer and for $\alpha = 20^\circ$, previously shown in Fig. 17, are also reported here for comparison. As expected on the basis of the results in Ref. [19], the Reynolds number at which the engulfment regime and the corresponding sudden increase of mixing take place progressively decreases as α becomes larger. For $\alpha = 10^\circ$ and 15°, the degree of mixing monotonically increases with Re

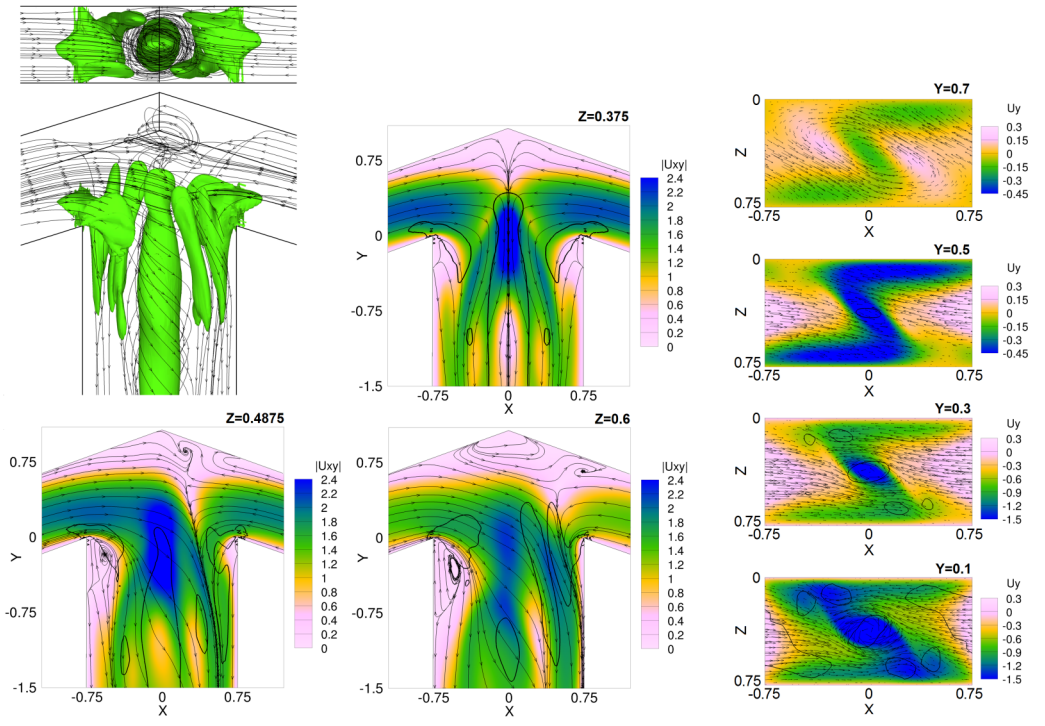

FIG. 16. Flow features in the top part of the arrow mixer with $\alpha = 20^\circ$ at Re $= 190$: (a) Isosurface of the λ_2 vortex indicator and velocity streamlines (top left), contours of the in-plane velocity magnitude, velocity streamlines, and trace of the isosurface of the λ_2 (thick line) for the sections at $Z = 0.375$ (top right), $Z = 0.4875$ (bottom left), and $Z = 0.6$ (bottom right); (b) contours of the y velocity, in-plane velocity vectors, and trace of the isosurface of the λ_2 (thick line) for the cross sections at (from top to bottom) $Y = 0.7$, $Y = 0.5$, $Y = 0.3$, and $Y = 0.1$.

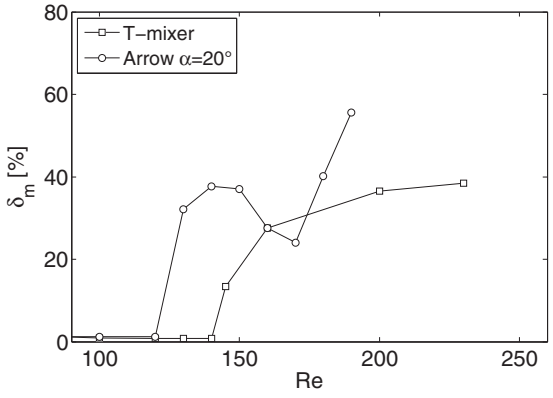

FIG. 17. Mixing degree as a function of the Reynolds number for the T-shaped micro-mixer and for the arrow-mixer with $\alpha = 20^\circ$.

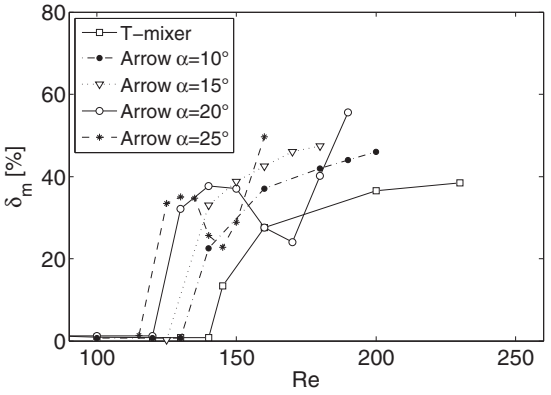

FIG. 18. Mixing degree as a function of the Reynolds number for the T-shaped micro-mixer and for the arrow mixers with different angles.

throughout the whole engulfment regime, as for T-mixers. The topology of the flow is indeed practically the same as for T-mixers, with the persistence of the top parts of the three-dimensional (3D) vortical structures near the upper walls of the mixer and of the two corotating stronger legs in the mixing channel for the whole engulfment regime. This can be seen, for instance, in Fig. 19 showing a isosurface of the λ_2 vortex indicator for $\alpha = 10^\circ$ at Re $= 180$ and 200. The λ_2 topology in the engulfment regime for T-mixers can be found, for instance, in Refs. [6,10,22,26]. Conversely, as for the previously analyzed configuration with $\alpha = 20^\circ$, the mixer with $\alpha = 25^\circ$ is characterized by a nonmonotonic behavior of the degree of mixing with Re. Also in this case, the decrease of mixing occurring at approximately Re $= 125$ is due to the same change in the flow topology as described in Sec. IV B, i.e., the disappearance of the top parts of the vortical structures and the consequent formation of a unique vortical structure in the mixing channel (see Fig. 20), which is less efficient in promoting mixing.

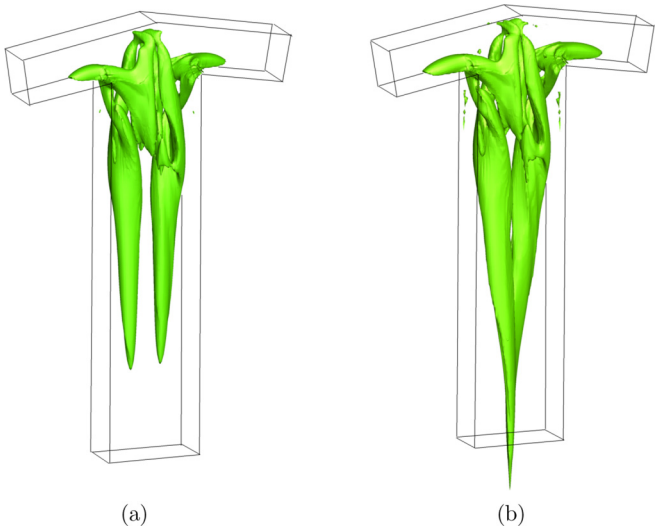

FIG. 19. Isosurface of the λ_2 vortex indicator for the arrow mixer with $\alpha = 10^\circ$. Simulations carried out at (a) Re $= 180$ and (b) Re $= 200$.

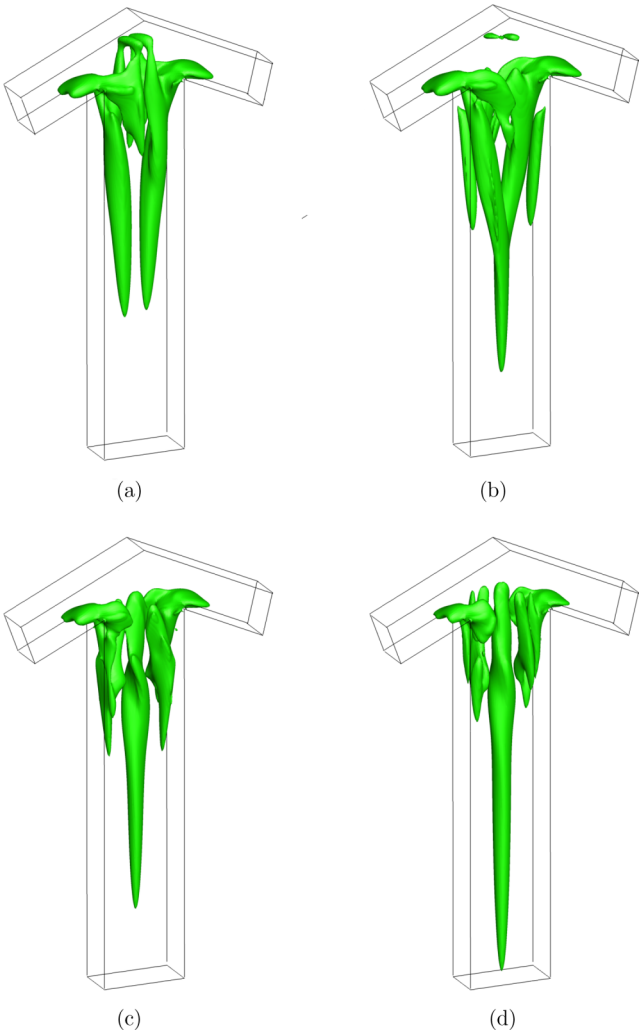

FIG. 20. Isosurface of the λ_2 vortex indicator for the arrow mixer with $\alpha = 25^\circ$. Simulations carried out at (a) Re = 130, (b) Re = 140, (c) Re = 150, and (d) Re = 160.

V. CONCLUDING REMARKS

The effect of Reynolds number on the liquid mixing in an arrow mixer has been analyzed by direct numerical simulations and flow visualizations. Although the latter did not use any confocal system, the signature of the flow regimes was well evident from the experimental images. Moreover, a proper comparison was possible between predictions and measurements, through the definition of postprocessing routines based on the evaluation of depth-averaged concentration maps. In all cases, the agreement between numerical results and flow visualizations was very good.

The engulfment regime was found to take place at a lower Reynolds number than for a T-mixer having the same cross section, and it was accompanied by a sharp improvement of the degree of mixing. However, when further increasing the Reynolds number, a reduction of the mixing performance was observed. Thanks to the availability of flow and vorticity fields from direct numerical simulations, it was ascertained that this is related to a deep change of the flow topology. In particular, the recirculation regions near the top of the mixer were found to move closer to the

top wall and to become weaker as the Reynolds number increases. At Re = 170, they completely disappear, with the liquid reaching the top part of the mixer undergoing a spiral pattern near the center of the mixing channel and being convected downward. This leads to the formation of a strong vortical leg in the mixing channel, constituted by the clinging of the two corotating vortical structures, that is less efficient in promoting mixing with respect to the classical engulfment regime, where these two corotating vortices remain instead separated. Indeed, the minimum of the mixer performance in the engulfment regime was found to take place at about Re = 170, with a mixing degree that was approximately half of the one at Re = 140. In particular, the degree of mixing was here even lower than the T-mixer one at the same Re. When further increasing the Re, the mixing degree augments again, because of the increase in size and strength of the unique vortical structure in the mixing channel. Finally, at Re = 200, this structure starts to oscillate, leading to an unsteady periodic flow. The sensitivity to the tilting angle has also been analyzed by means of numerical simulations. As expected, the value of the Reynolds number at which there is the onset of the engulfment regime and then sudden increase of mixing becomes progressively lower with increasing α. For low tilting angles ($\alpha = 10^\circ$ and 15°), the degree of mixing monotonically increases with Re throughout the whole steady engulfment regime, as for T-mixers. Conversely, for $\alpha = 25^\circ$, the behavior of the degree of mixing in nonmonotonic with Re, as for $\alpha = 20^\circ$, with a sudden decrease of mixing due to the same change in the flow topology as that observed for $\alpha = 20^\circ$.

Thus, arrow mixers are interesting because they trigger mixing at lower Re compared to T-mixers and this effect is more pronounced for larger tilting angles of the inlet channels. However, when the angle exceeds some critical value, which for the present configuration is between $\alpha = 15^\circ$ and 20°, the degree of mixing no longer increases monotonically with Re; therefore, careful control of the operating conditions is needed for these configurations.

ACKNOWLEDGMENTS

This work was supported by the University of Pisa through the "Progetti di Ricerca di Ateneo PRA 2017-2018" funding program. The authors wish also to thank CINECA computing center (Bologna, Italy) for allowance of computational resources under the ISCRA program (class B project "MIRE"). Moreover, the authors are grateful to Deborah Spaltro, Tommaso Pannuzi, Matteo Antognoli, and Cesare Merello.

[1] I. Rossetti and M. Compagnoni, Chemical reaction engineering, process design and scale-up issues at the frontier of synthesis: Flow chemistry, Chem. Eng. J. **296**, 56 (2016).

[2] X. Yao, Y. Zhang, L. Du, J. Liu, and J. Yao, Review of the applications of microreactors, Renewable Sustainable Energy Rev. **47**, 519 (2015).

[3] D. M. Roberge, L. Ducry, N. Bieler, P. Cretton, and B. Zimmermann, Microreactor technology: A revolution for the fine chemical and pharmaceutical industries? Chem. Eng. Technol. **28**, 318 (2005).

[4] V. Kumar, M. Paraschivoiu, and K. D. P. Nigam, Single-phase fluid flow and mixing in microchannels, Chem. Eng. Sci. **66**, 1329 (2011).

[5] C.-Y. Lee, W.-T. Wang, C.-C. Liu, and L.-M. Fu, Passive mixers in microfluidic systems: A review, Chem. Eng. J. **288**, 146 (2016).

[6] T. Andreussi, C. Galletti, R. Mauri, S. Camarri, and M. V. Salvetti, Flow regimes in T-shaped micromixers, Comput. Chem. Eng. **76**, 150 (2015).

[7] R. J. Poole, M. Alfateh, and A. P. Gauntlett, Bifurcation in a T-channel junction: Effects of aspect ratio and shear-thinning, Chem. Eng. Sci. **104**, 839 (2013).

[8] S. K. Reddy Cherlo and S. Pushpavanam, Effect of depth on onset of engulfment in rectangular microchannels, Chem. Eng. Sci. **65**, 6486 (2010).

[9] A. Soleymani, H. Yousefi, and I. Turunen, Dimensionless number for identification of flow patterns inside a T-micromixer, Chem. Eng. Sci. **63**, 5291 (2008).
[10] A. Fani, S. Camarri, and M. V. Salvetti, Investigation of the steady engulfment regime in a three-dimensional T-mixer, Phys. Fluids **25**, 064102 (2013).
[11] C. Galletti, M. Roudgar, E. Brunazzi, and R. Mauri, Effect of inlet conditions on the engulfment pattern in a T-shaped micro-mixer, Chem. Eng. J. **185–186**, 300 (2012).
[12] N. Kockmann, T. Kiefer, M. Engler, and P. Woias, Convective mixing and chemical reactions in microchannels with high flow rates, Sensors Actuators B: Chem. **117**, 495 (2006).
[13] C. Galletti, G. Arcolini, E. Brunazzi, and R. Mauri, Mixing of binary fluids with composition-dependent viscosity in a T-shaped micro-device, Chem. Eng. Sci. **123**, 300 (2015).
[14] G. Orsi, C. Galletti, E. Brunazzi, and R. Mauri, Mixing of two miscible liquids in T-shaped microdevices, Chem. Eng. Trans. **32**, 1471 (2013).
[15] L. Siconolfi, S. Camarri, and M. V. Salvetti, T-mixer operating with water at different temperatures: Simulation and stability analysis, Phys. Rev. Fluids **3**, 033902 (2018).
[16] H. V. Babu, S. Satu, M. Haderlein, W. Peukert, and N. Verma, Numerical investigation of flow patterns and concentration profiles in Y-mixers, Chem. Eng. Technol. **39**, 1963 (2016).
[17] N. Kockmann and D. M. Roberge, Transitional flow and related transport phenomena in curved microchannels, Heat Transfer Eng. **32**, 595 (2011).
[18] M. Rahimi, N. Azimi, M. A. Parsamogadam, A. Rahimi, and M. M. Masahy, Mixing performance of T, Y, and oriented Y-micromixers with spatially arranged outlet channel: Evaluation with Villermaux/Dushman test reaction, Microsystem Technol. **23**, 3117 (2017).
[19] L. Siconolfi, A. Fani, S. Camarri, and M. V. Salvetti, Effect of geometry modifications on the engulfment in micromixers: Numerical simulations and stability analysis, Eur. J. Mech. B **55**, 360 (2016).
[20] B. J. You, Y. Choi, and S. G. Im, Influence of adjusting the inlet channel confluence angle on mixing behavior in inertial microfluidic mixers, Microfluid. Nanofluid. **21**, 121 (2017).
[21] C. Galletti, E. Brunazzi, L. Siconolfi, D. Spaltro, and R. Mauri, Mixing performance of arrow-shaped micro-devices, Chem. Eng. Trans. **57**, 1309 (2017).
[22] A. Mariotti, C. Galletti, R. Mauri, M. V. Salvetti, and E. Brunazzi, Steady and unsteady regimes in a T-shaped micro-mixer: Synergic experimental and numerical investigation, Chem. Eng. J. **341**, 414 (2018).
[23] M. V. Salvetti, A. Mariotti, C. Galletti, and E. Brunazzi, Steady and unsteady regimes in a T-shaped micro-mixer: Synergic experimental and numerical investigation, in *Proceedings of the ASME 2018 5th Joint US-European Fluids Engineering Division Summer Meeting, FEDSM2018 July 15–20, 2018, Montreal, Quebec, Canada* (American Society of Mechanical Engineers, New York, NY, 2018), Vol. 3.
[24] P. F. Fischer, J. W. Lottes, and S. G. Kerkemeier, nek5000 web page, http://nek5000.mcs.anl.gov
[25] A. Fani, S. Camarri, and M. V. Salvetti, Unsteady asymmetric engulfment regime in a T-mixer, Phys. Fluids **26**, 074101 (2014).
[26] C. Galletti, A. Mariotti, L. Siconolfi, R. Mauri, and E. Brunazzi, Numerical investigation of flow regimes in T-shaped micromixers: Benchmark between finite volume and spectral element methods, Can. J. Chem. Eng. **97**, 528 (2019).
[27] J. Jeong and F. Hussain, On the identification of a vortex, J. Fluid Mech. **285**, 69 (1995).
[28] S. Dreher, N. Kockmann, and P. Woias, Characterization of laminar transient flow regimes and mixing in T-shaped micromixers, Heat Transfer Eng. **30**, 91 (2009).
[29] C. Galletti, E. Brunazzi, and R. Mauri, Unsteady mixing of binary liquid mixtures with composition-dependent viscosity, Chem. Eng. Sci. **164**, 333 (2017).